Simulations of the Eastern North Pacific Intraseasonal Variability in CMIP5 GCMs

XIANAN JIANG

Joint Institute for Regional Earth System Science and Engineering, University of California, Los Angeles, Los Angeles, and Jet Propulsion Laboratory, California Institute of Technology, Pasadena, California

ERIC D. MALONEY

Department of Atmospheric Science, Colorado State University, Fort Collins, Colorado

JUI-LIN F. LI AND DUANE E. WALISER

Jet Propulsion Laboratory, California Institute of Technology, Pasadena, California

ABSTRACT

As a key component of tropical atmospheric variability, intraseasonal variability (ISV) over the eastern North Pacific Ocean (ENP) exerts pronounced influences on regional weather and climate. Since general circulation models (GCMs) are essential tools for prediction and projection of future climate, current model deficiencies in representing this important variability leave us greatly disadvantaged in studies and prediction of climate change. In this study, the authors have assessed model fidelity in representing ENP ISV by analyzing 16 GCMs participating in phase 5 of the Coupled Model Intercomparison Project (CMIP5). Among the 16 CMIP5 GCMs examined in this study, only seven GCMs capture the spatial pattern of the leading ENP ISV mode relatively well, although even these GCMs exhibit biases in simulating ISV amplitude. Analyses indicate that model fidelity in representing ENP ISV is closely associated with the ability to simulate a realistic summer mean state. The presence of westerly or weak mean easterly winds over the ENP warm pool region could be conducive to more realistic simulations of the ISV. One hypothesis to explain this relationship is that a realistic mean state could produce the correct sign of surface flux anomalies relative to the ISV convection, which helps to destabilize local intraseasonal disturbances. The projected changes in characteristics of ENP ISV under the representative concentration pathway 8.5 (RCP8.5) projection scenario are also explored based on simulations from three CMIP5 GCMs. Results suggest that, in a future climate, the amplitude of ISV could be enhanced over the southern part of the ENP while reduced over the northern ENP off the coast of Mexico/Central America and the Caribbean.

1. Introduction

During boreal summer, convective activity over the eastern North Pacific Ocean (ENP) along the intertropical convergence zone (ITCZ) exhibits significant intraseasonal variability (ISV). Through its associated large-scale circulation and thermodynamical variations, the ISV exerts broad impacts on regional weather and climate systems, including the North American monsoon (NAM), midsummer drought over Central America, and Caribbean rainfall and low-level jet, as well as tropical cyclone activity over the ENP and the Gulf of Mexico (e.g., Magana et al. 1999; Maloney and Hartmann 2000a,b; Higgins and Shi 2001; Lorenz and Hartmann 2006; Small et al. 2007; Wu et al. 2009; Serra et al. 2010; Martin and Schumacher 2011). By modulating the activity of these climate/weather systems on an intraseasonal time scale, the ISV thus provides a foundation for extended-range prediction of the tropical atmosphere.

Two leading ISV modes associated with the ENP ITCZ have been previously reported with dominant periods of 40 days (hereafter a 40-day ISV mode) and 16 days [i.e., a quasi-biweekly mode (QBM)], respectively.

Corresponding author address: Dr. Xianan Jiang, Jet Propulsion Laboratory, California Institute of Technology, 4800 Oak Grove Dr., MS 233-300, Pasadena, CA 91109.
E-mail: xianan@jifresse.ucla.edu

The 40-day ISV mode over the ENP is largely considered a local expression of the global Madden–Julian oscillation (MJO) (Madden and Julian 1994; Maloney and Esbensen 2003), although recent modeling work suggests that similar 40-day ENP variability can exist when isolated from the Eastern Hemisphere (Jiang et al. 2012; Rydbeck et al. 2013). In addition to the eastward propagation, a northward-moving component of this mode is also noted (Jiang and Waliser 2008; Maloney et al. 2008; Small et al. 2011), exhibiting substantial similarity to its counterpart in the Asian summer monsoon (Jiang et al. 2004; Jiang and Waliser 2008). The second leading ISV mode over the ENP (i.e., QBM) exhibits a smaller spatial scale than the first ISV mode and is largely characterized by meridional propagation (Jiang and Waliser 2009).

While significant achievements have been made in modeling global ISV during past decades, significant challenges remain in current general circulation models (GCMs) (e.g., Slingo et al. 1996; Waliser et al. 2003; Lin et al. 2006; Kim et al. 2009). For ENP ISV, Lin et al. (2008) analyzed simulations of ISV and easterly waves over the ENP by the 22 phase 3 of the Coupled Model Intercomparison Project (CMIP3) models used in the Intergovernmental Panel on Climate Change (IPCC) Fourth Assessment Report (AR4). Their results indicate that the variance of ENP ISV tends to be underestimated in most of the CMIP3 GCMs. Meanwhile, the eastward propagation associated with observed ENP ISV is also poorly represented in these CMIP3 models. By applying an extended empirical orthogonal function (EEOF) technique, a recent analysis including many CMIP3-era models illustrated that, among the total of nine models examined, only two GCMs were able to realistically simulate both of the two observed leading ISV modes over the ENP (Jiang et al. 2012). Deficiencies of current GCMs in representing this important form of variability greatly limit our skill for extended-range prediction. Until very recently, useful predictive skill of the global ISV in most current GCMs had generally been limited to only 1–2 weeks (Waliser 2012), although the intrinsic period of the dominant mode of intraseasonal variability is about 40–50 days. Meanwhile, as GCMs have been essential tools for prediction and projection of climate changes, large model deficiencies in depicting this fundamental component of atmospheric variability leave us disadvantaged in undertaking climate change studies, particularly in projecting future activities of extreme events that are significantly modulated by ISV.

Building upon past successes of several model comparison project activities, the fifth phase of the CMIP Project (CMIP5) provides another state-of-the-art multimodel dataset to advance our knowledge of climate variability and climate change (Taylor et al. 2012). In this study, we assess CMIP5 model fidelity in representing ISV over the ENP and neighboring areas by analyzing 16 GCMs participating in CMIP5. This work is a part of the collective efforts coordinated by the CMIP5 Task Force of the National Oceanic and Atmospheric Administration (NOAA) Modeling, Analysis, Predictions, and Projections (MAPP) program.

The outline of this paper is as follows. In section 2, the CMIP5 models and observational datasets used for this study are briefly described. In section 3, we focus on examining how well the summer mean state and the leading ISV mode over the ENP are simulated by the 16 CMIP5 GCMs. We further analyze the projected changes in characteristics of ENP ISV in future climate based on simulations from three GCMs in section 4. Finally, a summary and a discussion are presented in section 5.

2. Model, datasets, and approaches

a. CMIP5 models

The CMIP5 experiments were conducted with more than 50 climate models representing 20 modeling groups with the aim of furthering our understanding of past and future climate change in key areas of uncertainty (Taylor et al. 2012). In this study, simulations from 16 atmosphere–ocean GCMs (AOGCMs) using a "historical" scenario are analyzed for the period of 1981–2005 to explore model fidelity in representing ENP ISV in the current climate. The historical forcings used to generate these runs include estimates of changes in atmospheric composition from natural and anthropogenic sources, volcanoes, greenhouse gases, and aerosols, as well as changes in solar output and land cover. The model names, institutes, and horizontal resolutions of the 16 AOGCMs used in our study are listed in Table 1. Additionally, simulations from three GCMs under the representative concentration pathway 8.5 (RCP8.5) projection scenario for the period of 2076–99 are analyzed to examine projected changes in the ENP ISV in future climate. RCP8.5 represents an extreme concentration pathway used for the CMIP5 project that features a continuous rise in radiative forcing during the twenty-first century, which leads to a value of about 8.5 W m^{-2} in 2100 (Riahi et al. 2011). The main variables analyzed in this study include precipitation, surface latent heat flux, and 850-hPa winds.

b. Observational datasets

Rainfall observations are based on the Tropical Rainfall Measuring Mission (TRMM product 3B42, version V6) (Huffman et al. 1995) precipitation dataset

TABLE 1. CMIP5 models analyzed in this study.

Model name	Modeling center	Horizontal resolution of atmospheric model (longitude × latitude in degrees)	Scenario
Second-generation Canadian Earth System Model (CanESM2)	Canadian Centre for Climate Modeling and Analysis	2.8 × 2.8	historical
Community Climate System Model, version 4.0 (CCSM4.0)	National Center for Atmospheric Research	1.25 × 1	historical
CNRM Coupled Global Climate Model, version 5 (CNRM-CM5)	Centre National de Recherches Météorologiques (CNRM), France	1.4 × 1.4	historical
CSIRO Mark, version 3 (CSIRO-Mk3)	Commonwealth Scientific and Industrial Research Organization (CSIRO), Australia	1.8 × 1.8	historical
GFDL Earth System Model with MOM4 ocean component (GFDL-ESM2M)	NOAA Geophysical Fluid Dynamics Laboratory (GFDL)	2.5 × 2.0	historical
Hadley Centre Coupled Model, version 3 (HadCM3)	UK Met Office Hadley Centre	3.7 × 2.5	historical
Hadley Centre Global Environmental Model, version 2 (Carbon Cycle) (HadGEM2-CC)		1.8 × 1.25	historical, RCP8.5
Hadley Centre Global Environmental Model, version 2 (Earth System) (HadGEM2-ES)		1.8 × 1.25	historical, RCP8.5
INM Coupled Model, version 4.0 (INM-CM4)	Institute for Numerical Mathematics (INM), Russia	2 × 1.5	historical
IPSL Coupled Model, version 5A, coupled with NEMO, low resolution (IPSL-CM5A-LR)	L'Institut Pierre-Simon Laplace (IPSL), France	3.75 × 1.8	historical
IPSL Coupled Model, version 5A, coupled with NEMO, medium resolution (IPSL-CM5A-MR)		2.5 × 1.25	
Model for Interdisciplinary Research on Climate Earth System Model (MIROC-ESM) and MIROC-ESM, chemistry coupled version (MIROC-ESM-CHEM)	Center for Climate System Research (University of Tokyo), National Institute for Environmental Studies, and Frontier Research Center for Global Change [Japan Agency for Marine–Earth Science and Technology (JAMSTEC)]	1.4 × 1.4	historical
MPI Earth System Model, low resolution (MPI-ESM-LR)	Max Planck Institute (MPI), Germany	1.9 × 1.9	historical, RCP8.5
MRI Coupled Atmosphere–Ocean General Circulation Model, version 3 (MRI-CGCM3)	Meteorological Research Institute (MRI), Japan	1.1 × 1.1	historical
Norwegian Earth System Model, version 1, medium resolution (NorESM1-M)	Norwegian Climate Center, Norway	2.5 × 1.9	historical

during the period from 1998 to 2010. TRMM 3B42 rainfall is a global precipitation product based on multi-satellite and rain gauge analyses. It provides precipitation estimates with 3-hourly temporal resolution on a 0.25° spatial resolution grid in a global belt between 50°S and 50°N. Daily wind fields during the period of the TRMM rainfall observations are obtained from the recent European Centre for Medium-Range Weather Forecasts (ECMWF) Interim Re-Analysis (ERA-Interim, hereafter ERA-I) (Dee et al. 2011), which has a horizontal grid resolution of 1.5° × 1.5°. Daily estimates of global latent heat flux fields on a 1° grid generated by the Woods Hole Oceanographic Institution (WHOI) objectively analyzed air–sea fluxes (OAFlux) project (Yu et al. 2008) are also analyzed to validate model latent heat flux patterns. The OAFlux product is determined from the best possible estimates of flux-related surface meteorology and state-of-the-art bulk flux parameterizations (Yu et al. 2008). Several satellite products are utilized in the OAFlux synthesis, including wind speed retrievals from both scatterometer and radiometer microwave remote sensing and SST daily high-resolution blended analysis by Reynolds et al. (2007), as well as a near-surface humidity product that was derived from Special Sensor Microwave Imager (SSM/I) column water vapor retrievals (Chou et al. 2001).

A common period of 1998–2010 is used for the observations because of the relatively short record of the TRMM rainfall dataset. In addition, all daily variables based on both observations and model simulations were interpolated to a common 2.5° × 2.5° grid system.

3. Simulations of the ENP ISV in CMIP5 GCMs under a historical scenario

a. Summer mean state

In this part of the study, model fidelity in representing the summer mean state over the ENP and adjacent regions is first assessed by analyzing output from 16 CMIP5 GCMs under the historical forcing scenario. Figure 1 displays summer mean (May–October) rainfall and 850-hPa winds for observations and the GCM simulations. Observed summer mean rainfall (Fig. 1a) is largely characterized by an elongated rain belt along the ENP ITCZ near 10°N, extending into the NAM region along the Sierra Madre Occidental off the Gulf of California. A rainfall maximum center over northern South America is also present. In conjunction with this rainfall pattern, a prominent feature in the observed 850-hPa wind fields over the ENP is the convergent flow onto the ITCZ, namely, the northeasterly winds to the north and the southeasterly winds and cross-equatorial flow to the

south of the ITCZ. It is noteworthy that very weak winds at 850 hPa are largely observed over the far eastern portion of the ENP, where the maximum summer rainfall resides, and even include a westerly component. At the surface, southwesterly mean winds occur in the region of the warm pool precipitation maximum (not shown), a basic state flow that has been argued to be important for the dynamics of ISV in this region given its influence on the sign of flux anomalies for a given signed surface wind anomaly (e.g., Maloney and Esbensen 2007).

All the GCMs generally capture the bulk features of the ITCZ rain belt, the NAM, and rainfall over South America, as well as associated 850-hPa wind patterns. (Note that daily 850-hPa wind based on historical simulations from CCSM4.0 and HadGEM2-ES were not available at the CMIP5 data portal at the time of analysis.) Significant model deficiencies are also discernible. In several GCMs, the rainfall maximum along the ENP ITCZ is displaced to the west side of the ENP rather than the far eastern part of the ENP as in the observations. The models that display this bias include CCSM4.0, GFDL-ESM2M, INM-CM4, both IPSL-CM5A GCMs, both MIROC-ESM GCMs, and NorESM1-M. Meanwhile, the amplitude of mean rainfall, particularly over the coastal region near Central America, is overestimated in several GCMs, which could be due in part to the relatively coarse resolutions in these GCMs that may create difficulties in resolving the finescale topographic features near the coast.

While more objective evaluations of mean rainfall and 850-hPa wind patterns in these GCMs will be illustrated in Fig. 2, it is worth mentioning that obvious deficiencies in simulated 850-hPa zonal wind patterns over the ENP ITCZ along 10°N are apparent in Fig. 1 in many GCMs. In contrast to relatively weak easterly, or even westerly, winds at 850 hPa over the ENP ITCZ in the observations as shown in Fig. 1a, strong easterly winds are detected in almost half of the 16 GCMs analyzed. Table 2 illustrates the domain-averaged summer mean zonal wind at 850 hPa over the ENP ITCZ region (5°–25°N, 140°–80°W) in observations and the GCM simulations. As will be further illustrated below, the biases in representing the summer mean low-level winds over the ENP in a GCM appear to be closely linked to the model deficiencies in simulating local intraseasonal variability.

Note that different periods were applied when calculating the summer mean state for observations (1998–2010) and GCMs (1981–2005). Therefore, the differences in mean rainfall and 850-hPa wind patterns between observations and models as shown in Fig. 1 could be partially associated with decadal variations in these fields. A sensitivity test performed by deriving summer
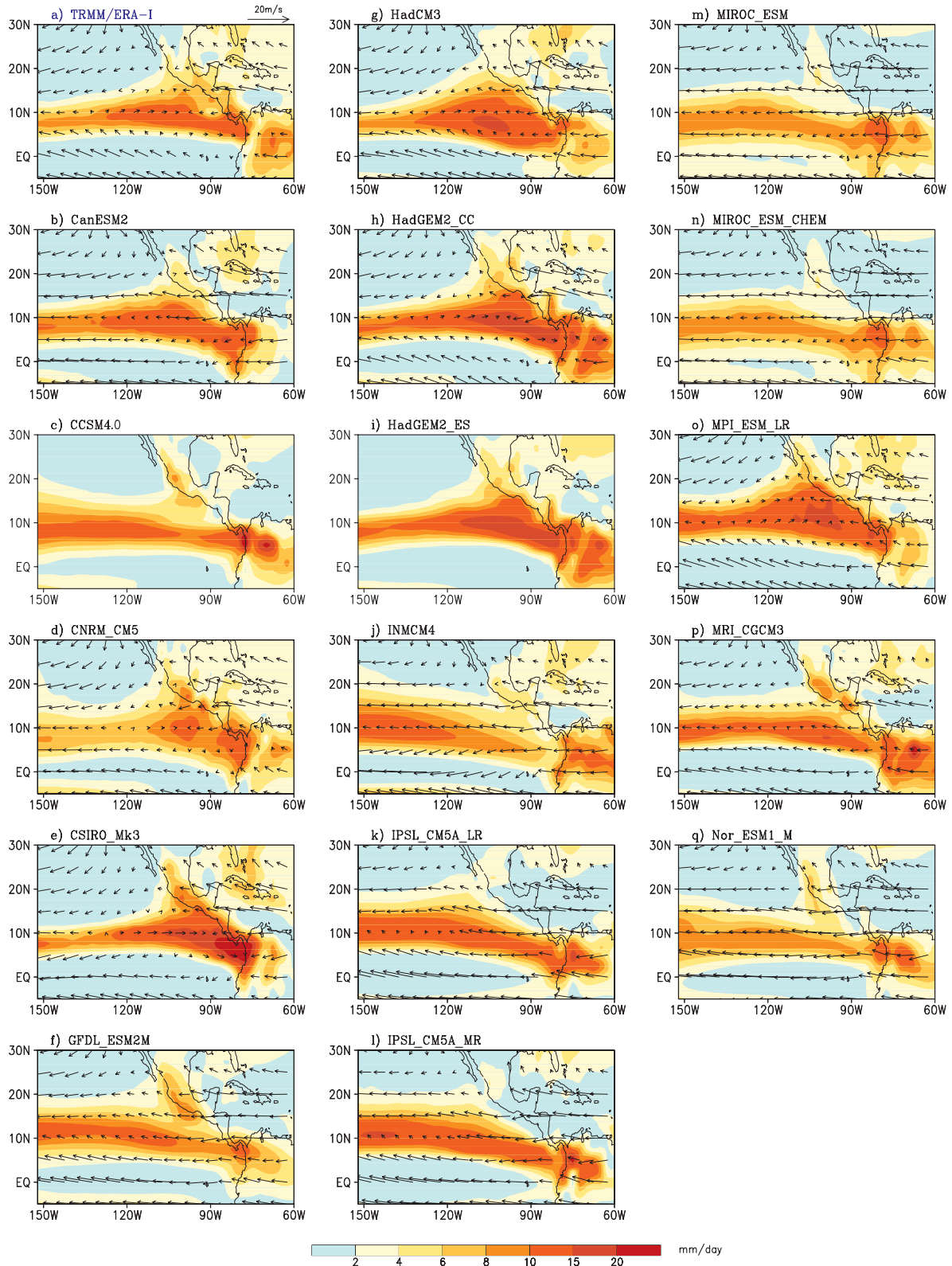
FIG. 1. (a) Observed and (b)–(q) simulated summer mean (May–October) rainfall patterns (shaded; see color bar at the bottom) and 850-hPa winds [vectors; see reference vector above (a)]. Observed rainfall and winds are based on TRMM and ERA-I for the period of 1998–2010, while model mean state is derived from historical simulations based on GCMs for the period of 1981–2005.
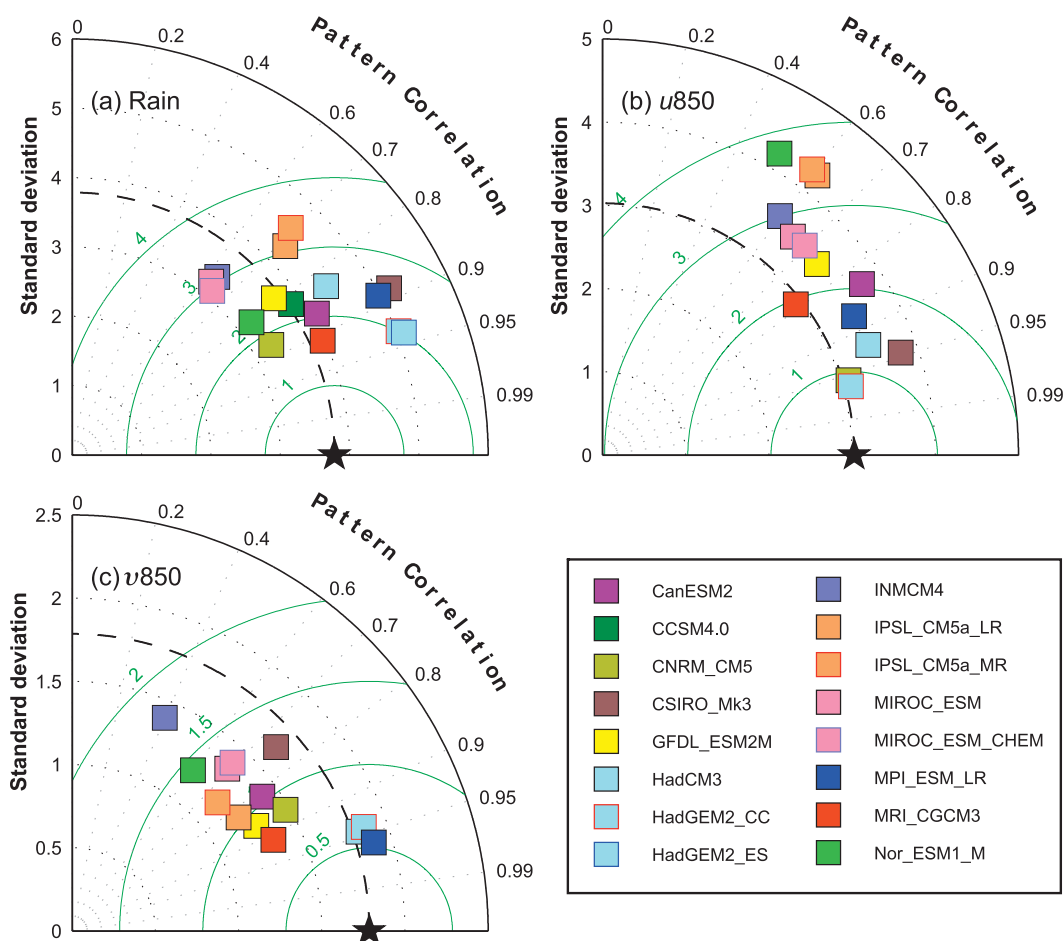
FIG. 2. Taylor diagrams for summer mean (May–September) (a) precipitation, (b) 850-hPa *u*-wind, and (c) 850-hPa
v-wind over the ENP (5°S–30°N, 150°–80°W) simulated in CMIP5 GCMs.

mean patterns for both observations and GCMs based on a common period of 1998–2005, however, illustrates very similar mean distributions in both rainfall and 850-hPa wind patterns to those in Fig. 1 in each dataset (not shown here), although slight differences can be noted in the amplitudes of mean patterns when a shorter period of data is used. Thus, the differences in the summer mean rainfall and 850-hPa wind patterns between the observations and GCMs shown in Fig. 1 are largely caused by model deficiencies, which could be associated with model schemes that represent cumulus convection, planetary boundary layer (PBL) mixing, cloud–radiation feedbacks, and/or SST biases from the inclusion of the atmosphere–ocean coupling (e.g., Sheffield et al. 2012, submitted to *J. Climate*).

Figure 2 presents an objective assessment of the summer mean state simulated in each CMIP5 GCM by illustrating Taylor diagrams for rainfall and wind patterns over the ENP domain (5°S–30°N, 150°–80°W). Taylor diagrams provide a way of quantifying how

closely a simulated pattern matches its observational counterpart in terms of their pattern correlation, centered root-mean-square (RMS) difference, and the amplitude of their standard deviations (Taylor 2001). For rainfall patterns (Fig. 2a), while the two HadGEM2 models (HadGEM2-CC and HadGEM2-ES) display the largest pattern correlations against the observations with correlation scores of about 0.93, the MRI-CGCM3 has the smallest RMS because of its better skill in simulating the spatial standard deviations of summer mean rainfall over the ENP. In addition, four other GCMs, including CSIRO-Mk3, MPI-ESM-LR, CanESM2, and CNRM-CM5, also exhibit relatively good pattern correlation scores relative to other GCMs. Performance in simulating summer mean rainfall in a GCM is largely consistent with that for the circulation pattern at 850 hPa. In general, models with relatively higher skill in simulating the summer mean rainfall pattern also exhibit better skill for the 850-hPa wind pattern, particularly in the zonal wind component (Figs. 2b,c).

TABLE 2. Summer mean zonal wind speed at 850 hPa over the ENP (5°–25°N, 140°–80°W) in observations and GCM simulations.

	Mean zonal wind speed (m s^{-1})
Observations	0.63
CanESM2	−4.02
CCSM4.0	n/a
CNRM-CM5	−0.77
CSIRO-Mk3	1.11
GFDL-ESM2M	−4.2
HadCM3	−0.6
HadGEM2-CC	0.2
HadGEM2-ES	n/a
INM-CM4	−6.5
IPSL-CM5A-LR	−6.1
IPSL-CM5A-MR	−6.6
MIROC-ESM	−6.4
MIROC-ESM-CHEM	−5.9
MPI-ESM-LR	0.42
MRI-CGCM3	−1.45
NorESM1-M	−9.2

Nevertheless, less defined stratification in model skill among the GCMs is found in simulated summer mean rainfall patterns than for winds.

Figure 3 illustrates the probability distribution function (PDF) of summer rainfall as a function of rain rate over the ENP ITCZ region (5°–15°N, 130°–90°W) for both TRMM observations and GCM simulations. This analysis was based on summertime (May–October) daily mean rainfall at each 2.5° × 2.5° grid point during the periods of 1981–2005 and 1998–2010 for model simulations and observations, respectively. The PDFs were derived by aggregating rain rates into logarithmically spaced histogram bins and were normalized by the total numbers of grid cells. Considering the limitation of TRMM in detecting weak rain and the model difficulty in simulating the frequency of no-rain days, only rainy grid cells with daily mean rainfall greater than 0.5 mm day^{-1} were included in deriving these PDFs. Results based on TRMM observations indicate that the largest frequency of daily mean rainfall occurs at 10 mm day^{-1} (Fig. 3a; note that rain rate on the x axis in Fig. 3 is on a log scale, a rain rate of 10 mm day^{-1} corresponds to 1 on the x axis.). While the frequency of occurrence peak at about 10 mm day^{-1} is generally captured in most of the GCMs, the observed rainfall PDF shape is reasonably well captured by only a very limited number of models, including HadGEM2-CC, HadGEM2-ES, and MRI-CGCM3. Precipitation in most of the other GCMs tends to fall in a narrow rain-rate range centered at 10 mm day^{-1}. The observed frequency in both very heavy and light rainfall regimes is generally underestimated in these models. An extreme example is found in the INM-CM4 (Fig. 3j), in which the rainfall over the ENP largely occurs in a range between 3 and 18 mm day^{-1}, in contrast to the much broader PDF in the observations. Very similar model biases in simulating summer rainfall PDFs are found over the equatorial Indian Ocean and western Pacific sectors in these CMIP5 GCMs (not shown here). These model biases are generally consistent with those discussed in previous studies (e.g., Lin et al. 2006; Thayer-Calder and Randall 2009), which suggests that model convection is triggered too often, resulting in persistent light rain rather than intense precipitation. These model biases in capturing convection PDFs are generally attributed to weaknesses in representing critical dependencies for convection on environmental parameters, such as moisture (e.g., Kim et al. 2009; Zhu et al. 2009), or lack of important self-suppression processes of deep convection, for example, convective and mesoscale downdrafts (Lin et al. 2006) and rainfall reevaporation (Kim et al. 2012).

b. Intraseasonal variability over the ENP

In this section, we proceed to examine how intraseasonal variability over the ENP is simulated in CMIP5 GCMs. Figure 4 illustrates general intraseasonal variability amplitude in both observations and CMIP5 GCM simulations by showing the standard deviations (STDs) of 10–90-day bandpass-filtered summertime (May–October) rainfall in each dataset. In TRMM, intraseasonal variability in precipitation generally maximizes in regions of high mean precipitation (Fig. 2), although intraseasonal variability is slightly displaced toward the Mexican coast relative to the mean precipitation distribution. ISV in the ENP is greatly underestimated in INM-CM4 and the two MIROC-ESM models. Relatively weak ISV amplitudes are also noticed in Can-ESM2, GFDL-ESM2M, and NorESM1-M. In contrast, ISV is simulated too strongly in the two HadGEM2 and the two IPSL-CM5A GCMs. Meanwhile, maximum ISV activity is centered over the western part of the ENP in CCSM4.0, GFDL-ESM2M, INM-CM4, the two IPSL-CM5A GCMs, and NorESM1-M, rather than over the eastern part of the ENP, as in the observations. This analysis indicates that the ability to capture the overall level of intraseasonal variability in the eastern Pacific varies widely across models. In addition, the ability of models to simulate intraseasonal wind variance generally tracks their ability to simulate intraseasonal precipitation variance (not shown).

Next, in order to identify the leading ISV modes over the ENP in both observations and GCM simulations, a complex empirical orthogonal function (CEOF) analysis was conducted for rainfall fields following the method
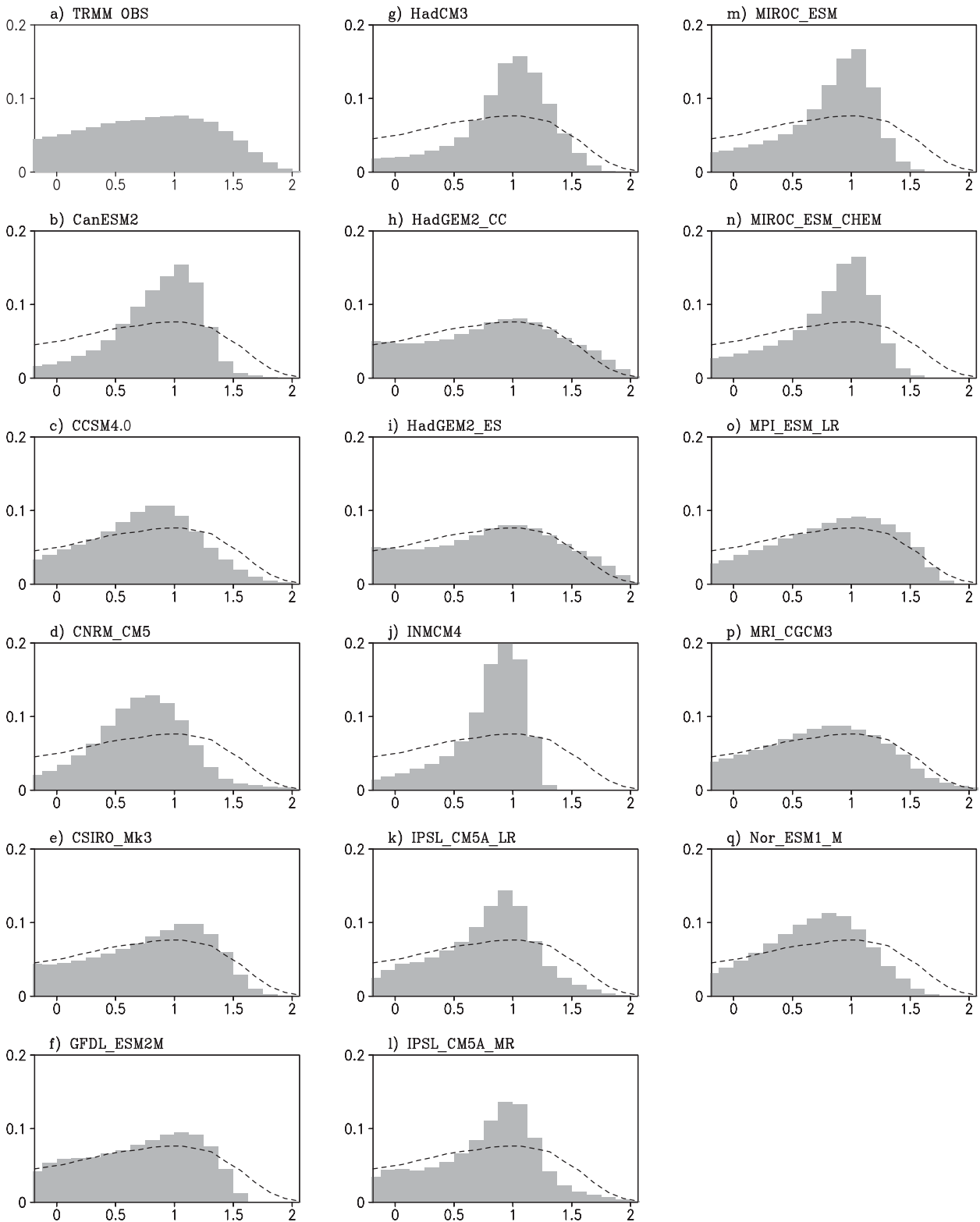
FIG. 3. (a) The PDF of summer rainfall over the ENP (5°–15°N, 130°–90°W) as a function of rain rate based on observations (gray bars). (b)–(q) The observed PDF is duplicated with black dashed lines and presented alongside GCM simulations (gray bars). The rain rate on the x axis is plotted on a log scale.
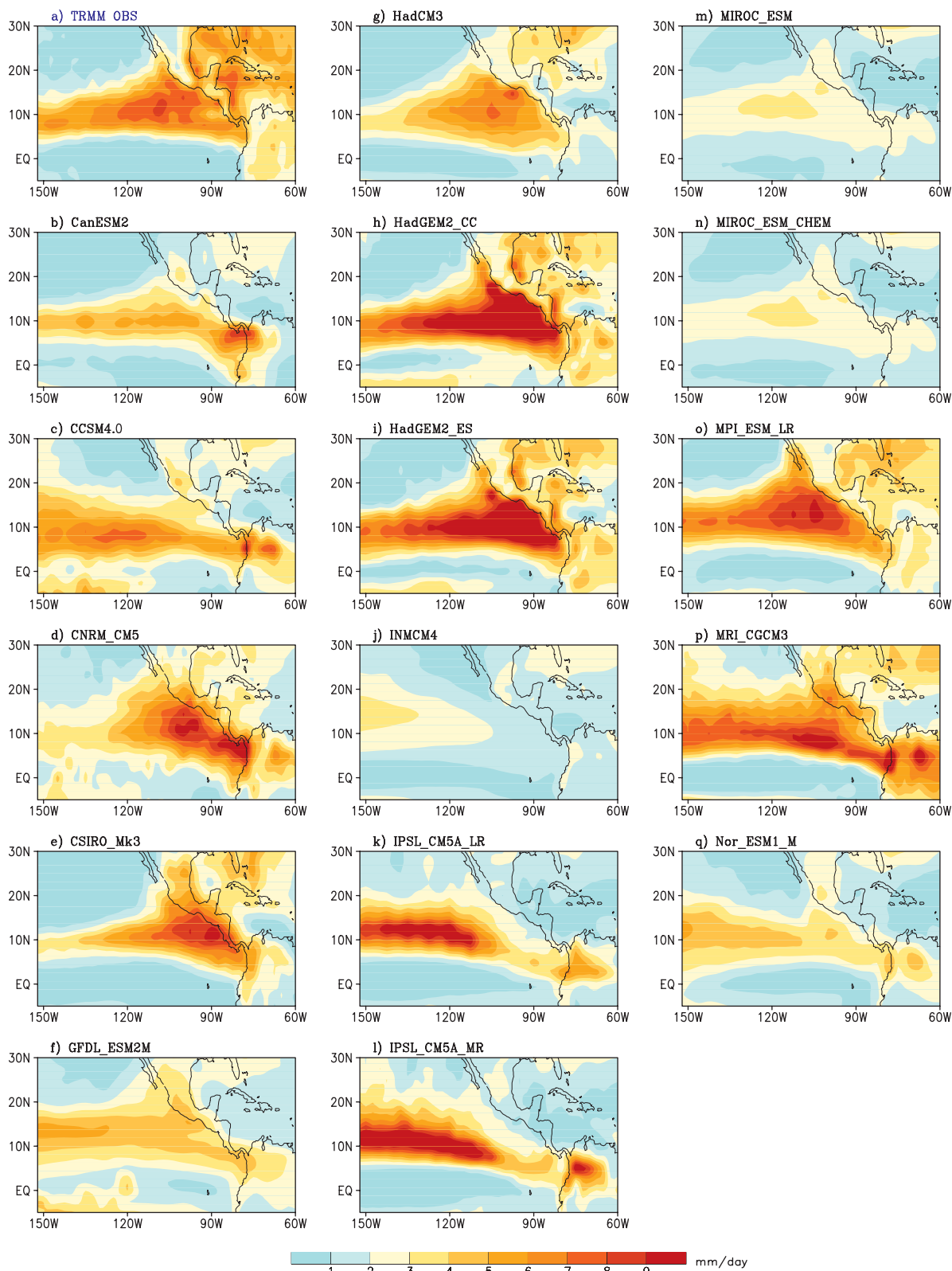
FIG. 4. The STD of 10–90-day bandpass-filtered summertime (May–September) rainfall based on (a) observations and (b)–(q) CMIP5 model simulations (mm day^{-1}).

of Maloney et al. (2008). In CEOF analysis, the co-variance matrix is constructed from the complex analytic function at each grid point consisting of the filtered time series of data plus i times its quadrature function, where the quadrature function is determined through a Hilbert transform. The resulting CEOFs are complex, and thus, an advantage of CEOF analysis is that a propagating signal can be represented by one CEOF (Barnett 1983; Horel 1984; Maloney et al. 2008) rather than a quadrature pair of EOFs, as in the traditional EOF approach or the extended EOF (EEOF) method, as adopted by Jiang et al. (2012), to identify the two leading ENP ISV modes. Considering dominant influences of the 40-day ISV mode, as well as greater model uncertainty in representing the observed QBM over the ENP, particularly in relatively coarse-resolution GCMs as suggested by Jiang et al. (2012), in the present study we examine CMIP5 model fidelity in representing the 40-day ISV mode over the ENP. Prior to the CEOF analyses, daily rainfall fields based on both TRMM observations and GCM simulations are subject to 30–90-day bandpass filtering. CEOF analyses are then applied to daily rainfall anomalies from the model and observational datasets over the ENP domain (5°–25°N, 140°–80°W) during boreal summer (June–September).

Spatial patterns of the amplitude of the first CEOF mode (CEOF1) based on TRMM observations and GCM simulations are illustrated in Fig. 5. Similar to the behavior illustrated by Maloney et al. (2008), the maximum amplitude of the observed rainfall CEOF1 occurs over the far eastern part of the ENP (Fig. 5a). The spatial amplitude of the CEOF1 is rather weak in Can-ESM2, CCSM4.0, GFDL-ESM2M, INM-CM4, the two MIROC-ESM models, and NorESM1-M, in general agreement with the weak amplitude in the STD patterns of 10–90-day bandpass-filtered rainfall anomalies in these models, shown in Fig. 4. A westward shift of the maximum amplitude relative to the observations is again evident in CCSM4.0, INM-CM4, and the two IPSL-CM5A models. While the two HadGEM2 models capture the observed spatial distribution of the amplitude pattern well, the CEOF1 amplitudes are stronger than observed. The MPI-ESM-LR, CNRM-CM5, and CSIRO-Mk3 models produce approximately the correct amplitude and spatial distribution of the leading CEOF mode.

Figure 6 presents observed and GCM-simulated spatial phase patterns of the CEOF1 mode over the ENP. To make the spatial phase patterns of CEOF1 based on the observations and simulations comparable to each other, the spatial phase of CEOF1 based on each dataset is adjusted by setting the domain-averaged phase to zero over the region of 10°–15°N, 110°–100°W. Contours of

spatial patterns based on each dataset are only displayed where local variances explained by CEOF1 exceed 8%. Note that the direction of propagation associated with the CEOF1 is indicated by the gradient of the spatial phase. Figure 6a illustrates the spatial phase pattern of the observed rainfall CEOF1 after the phase adjustment. In accord with previous studies, the observed leading ISV mode over the ENP associated with the CEOF1 largely exhibits eastward propagation, although a northward component is also evident (e.g., Jiang and Waliser 2008; Maloney et al. 2008; Jiang et al. 2012). The observed northeastward propagation associated with the leading ISV mode over the ENP, as illustrated by the spatial phase pattern based on TRMM, is reasonably well captured in several models, including CNRM-CM5, CSIRO-Mk3, GFDL-ESM2M, HadCM3, HadGEM2-CC, HadGEM2-ES, MPI-ESM-LR, and MRI-CGCM3, although the northward-propagating component in the two HadGEM2 models dominates the eastward component. In contrast to the eastward propagation in the observations, westward propagation associated with CEOF1 is seen in several GCMs, including CanESM2, INM-CM4, the two IPSL-CM5A GCMs, and the two MIROC-ESM models.

The fidelity in simulating the leading ENP ISV mode by each CMIP5 model is then objectively assessed by calculating the pattern correlation of the simulated rainfall CEOF1 against its observed counterpart. To increase sampling when assessing the model skill scores, spatial patterns of rainfall anomalies associated with the CEOF1 based on both observations and GCM simulations are derived at two quadratic phases by multiplying the CEOF1 amplitude by the cosine and sine of the spatial phase on each grid point, respectively. Pattern correlations between the observed and simulated CEOF1 anomalous rainfall patterns over the ENP domain are then calculated at both of these two quadratic phases. A final pattern correlation score for a particular model in simulating the spatial pattern of the CEOF1 is derived by averaging these two pattern correlation coefficients. Figure 7 shows pattern correlation scores in depicting the CEOF1 rainfall pattern (x axis) versus ENP domain-averaged (5°–25°N, 140°–80°W) CEOF1 amplitude relative to the observed counterpart (y axis) in each model simulation. It is shown that a majority of the CMIP5 models tend to underestimate the amplitude of the leading ENP ISV mode associated with the rainfall CEOF1, except for CNRM-CM5, MPI-ESM-LR, and the two versions of HadGEM2. Also note that seven GCMs, including MRI-CGCM3, MPI-ESM-LR, CSIRO-Mk3, CNRM-CM5, and three versions of Hadley Centre GCMs (i.e., HadCM3, HadGEM2-CC, and HadGEM2-ES) exhibit relatively high skill scores in capturing the CEOF1 patterns, with
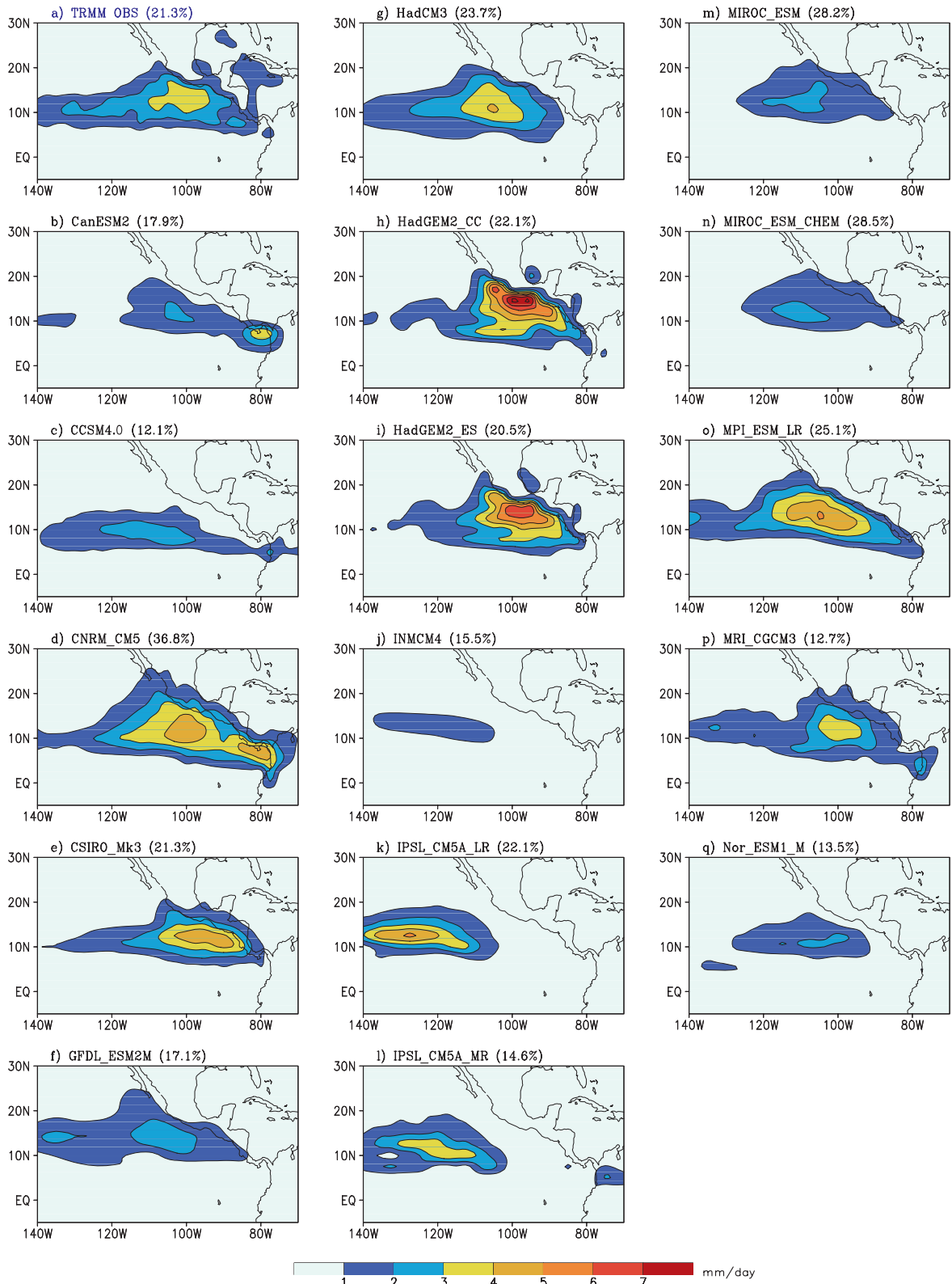
FIG. 5. Spatial distribution of amplitude of the CEOF1 mode of 30–90-day bandpass-filtered rainfall during boreal summer (June–September) over the ENP based on (a) observations and (b)–(q) model simulations. Percentages of variances explained by the CEOF1 in observations and GCMs are labeled above the corresponding panels.
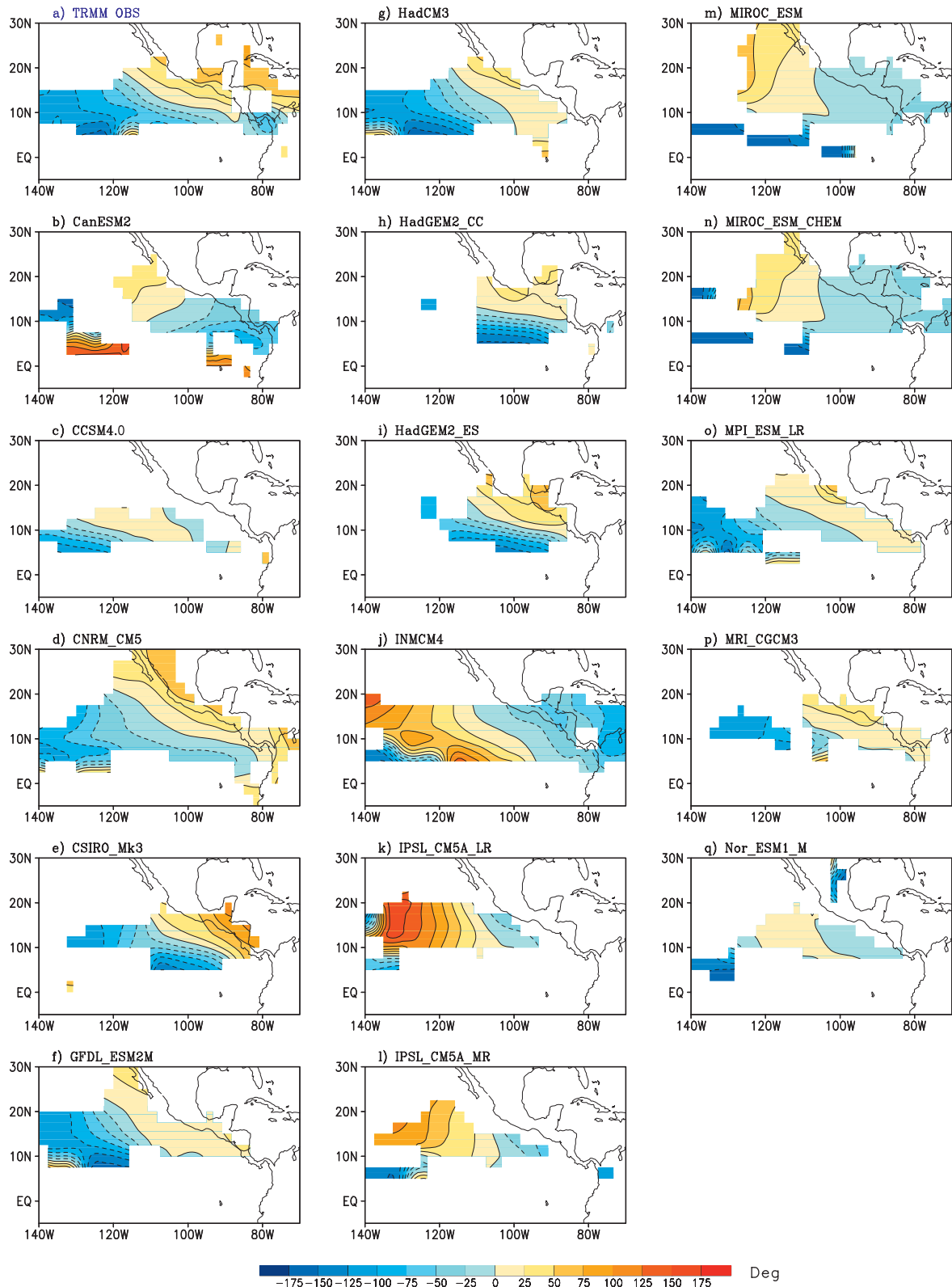
FIG. 6. As in Fig. 5, but for spatial distribution of phase of the summertime rainfall CEOF1 mode over the ENP. The spatial phase based on each dataset is adjusted by setting the domain-averaged value to be zero over the box region of 10°–15°N, 110°–100°W. Contours are only displayed over grids with local variances explained by CEOF1 exceeding 8%.
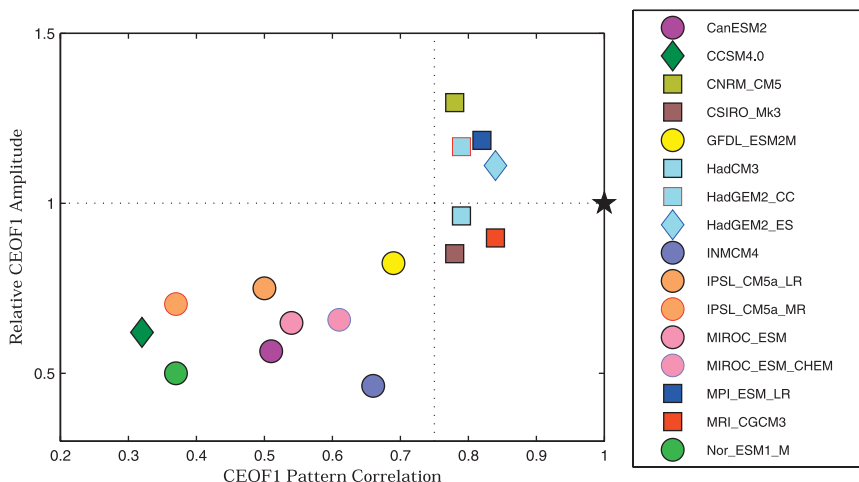
FIG. 7. The x axis shows pattern correlation coefficients of the CEOF1 mode between TRMM observations and CMIP5 GCM simulations. The y axis shows relative amplitudes of CEOF1 in model simulations to the observed counterpart. Both pattern correlations and amplitudes are derived by averaging over the area of 5°–25°N, 140°–80°W where the active ISV is observed. The black star represents the TRMM observations. Models represented by squares display westerly or weak easterly (<1.5 m s^{-1}) summer mean wind at 850 hPa, while strong easterly winds (>4 m s^{-1}) are noted in models represented by circles. Wind fields are not available in the data portal at the time of this analysis from the two GCMs represented by diamonds.

correlation scores exceeding 0.75. Figure 7 succinctly illustrates that the CMIP5 models exhibit widely different abilities simulating intraseasonal variability in the ENP.

To show an example of how the spatial evolution associated with the leading ENP ISV modes are simulated in GCMs, Fig. 8 illustrates the evolution of patterns of anomalous rainfall and 850-hPa winds associated with the ENP ISV in the observations and the five GCMs that exhibit relatively better pattern correlation scores in representing the observed CEOF1, as illustrated in Fig. 7. The evolution of anomalous rainfall and 850-hPa winds in both observations and model simulations are derived by lag regression against rainfall anomalies averaged over a small domain over the ENP (7.5°–15°N, 110°–100°W; see the small red box in the top panel of Fig. 8a). Note that 30–90-day bandpass filtering was applied to all these fields prior to calculation of the regression patterns. In agreement with previous studies (e.g., Maloney and Esbensen 2003, 2007; Jiang and Waliser 2008; Jiang et al. 2012), Fig. 8a largely captures the main features of the observed 40-day ISV mode over the ENP. An eastward-propagating signal that impinges from the west is clearly seen. Enhanced convection over the ENP is found to be associated with anomalous low-level southwesterly winds. These prominent features of the observed leading ISV mode over the ENP are largely captured in these several GCMs that produce good intraseasonal simulations based on Fig. 7.

Next, similar to Jiang et al. (2012), the linkage between the ENP ISV and the eastward-propagating MJO over the Indian Ocean and western Pacific is further explored. Figure 9 illustrates zonal propagation associated with the leading ISV mode over the ENP based on both observations and GCMs by displaying longitude–time profiles of rainfall anomalies averaged between 10°S and 15°N. As in Fig. 8, these time evolution patterns of anomalous rainfall associated with the leading ENP ISV in each dataset were derived by lag regression against rainfall over the eastern Pacific box in Fig. 8a. In agreement with the previous discussion, an eastward propagation with a phase speed of about 4 m s^{-1} in the eastern Pacific is clearly evident in observations (Fig. 9a). This observed eastward propagation associated with the leading ISV mode is reasonably well captured in the several models that exhibit relatively higher skill scores, as illustrated in Fig. 7, including CNRM-CM5, CSIRO-Mk3, the three Hadley Centre GCMs, MPI-ESM-LR, and MRI-CGCM3. Very weak or westward-propagating signals are simulated in other GCMs, with relative lower scores for ENP ISV.

Particularly noteworthy of Fig. 9 is that in observations, the ENP ISV is clearly linked to eastward-propagating signals from the Indian Ocean/western Pacific sector (Fig. 9a). This tends to support the notion that the ENP ISV could be a local expression of the circumnavigating MJO signals that propagate into the eastern Pacific. This
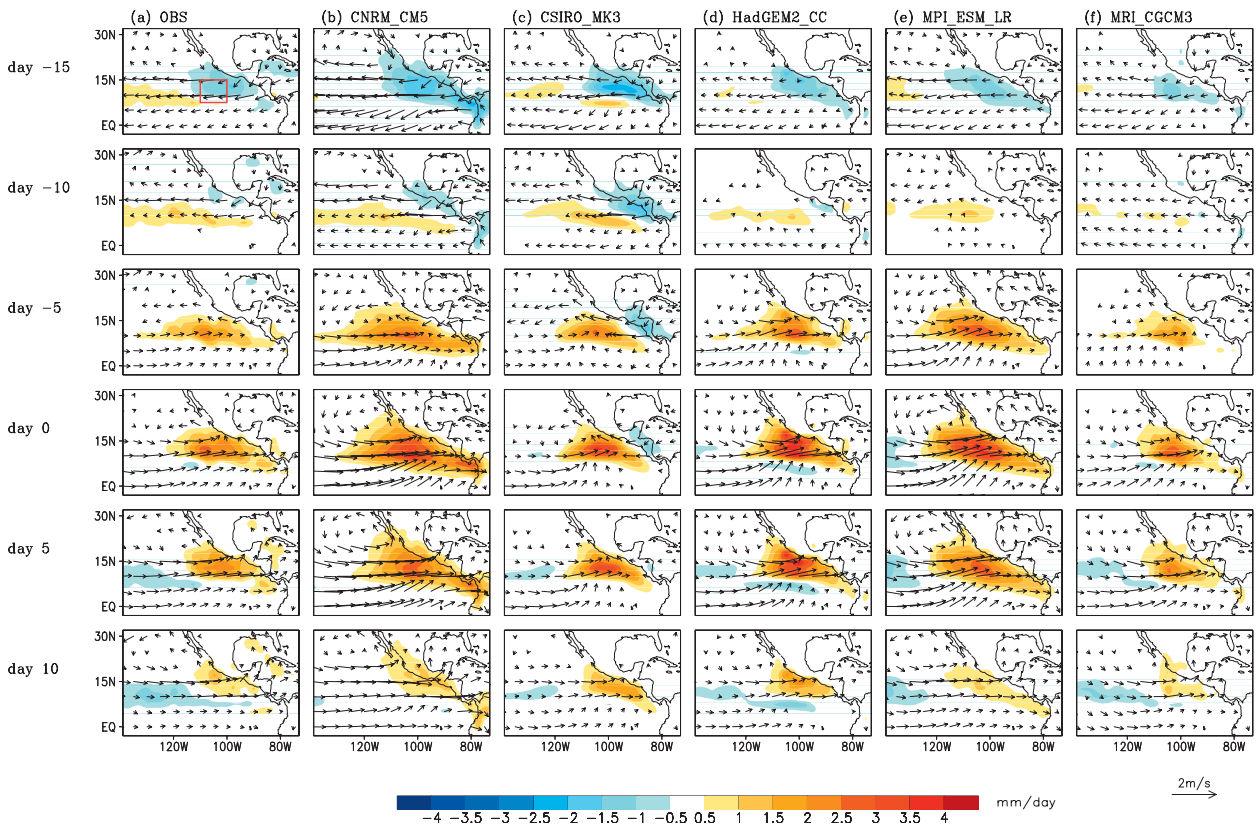
FIG. 8. Evolution of anomalous rainfall (shaded) and 850-hPa winds (vectors) associated with the dominant ISV mode over the ENP as derived by lag regressions against the corresponding rainfall anomalies over 7.5°–15°N, 110°–100°W [see the red box in the top panel of (a)] based on (a) observations and (b)–(f) CMIP5 model simulations.

also explains why a typical evolution of ENP ISV could be obtained by lag regression against a global MJO index as described by Maloney and Esbensen (2003). In contrast, the observed linkage between ENP ISV and propagating signals from the western Pacific is only captured by two GCMs, that is, CNRM-CM5 and MPI-ESM-LR. While ENP ISV is relatively well simulated in CSIRO-Mk3, the three Hadley Centre models, and MRI-CGCM3, it tends to be independent from the forcing from the Eastern Hemisphere in these model simulations. These results largely agree with those by Rydbeck et al. (2013) and Jiang et al. (2012) and indicate that ENP ISV could represent an unstable regional mode of variability that exists in isolation from the western Pacific given the local eastern Pacific summer mean state.

It is also noted that the models with relatively better skill in representing the leading ENP ISV mode also tend to exhibit better skill at simulating summer mean rainfall and 850-hPa wind patterns (cf. Figs. 1, 7). Further inspection of the summer mean 850-hPa zonal wind (Table 2) illustrates that a common feature among these GCMs with relatively higher skill in simulating ENP ISV is the presence of westerly or very weak easterly mean

winds (less than 1.5 m s^{-1}) over the ENP warm pool region, as in the observations. In contrast, most GCMs with relatively poor skill in simulating ISV exhibit a stronger easterly summer mean low-level flow (greater than 4 m s^{-1}). In Fig. 7, models with a westerly or very weak easterly summer mean 850-hPa winds over the ENP are labeled with "square" marks, while those with strong easterly summer mean winds with "circle" marks. (Note that daily wind data were not available from the CMIP5 data portal at the time of this analysis for the two models with "diamond" marks.) A close association between summer mean 850-hPa zonal wind and model performance in representing the leading ENP ISV mode is readily seen in Fig. 7. All the GCMs (except HadGEM2-ES because of missing wind data) that show pattern correlation scores greater than 0.75 are characterized by westerly or weak easterly summer mean winds at 850 hPa. Therefore, these results strongly suggest that a realistic representation of the mean state could be conducive for improved simulations of the ENP ISV, which has also been discussed for the MJO simulations over the western Pacific and Indian Ocean (e.g., Inness and Slingo 2003; Sperber et al. 2005; Kim et al. 2009, 2011).
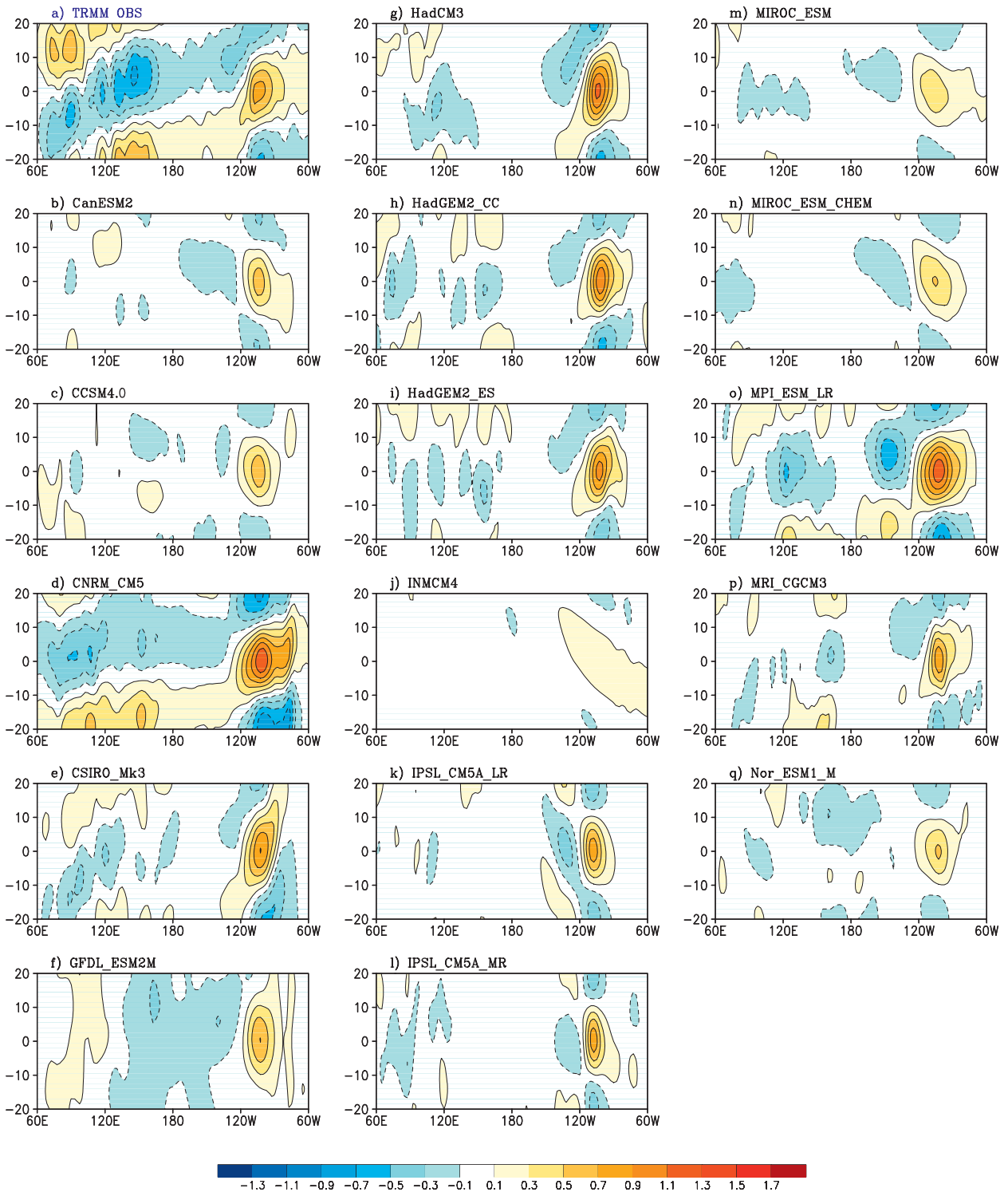
FIG. 9. (a) Observed and (b)–(q) simulated longitude–time evolution of rainfall anomalies associated with the dominant ISV mode over the ENP. The *y* axis provides time in days. Rainfall anomalies in each panel are averaged between 10°S and 15°N.

One hypothesis for the close linkage between model performance in simulating the ISV and the low-level mean flow over the ENP is that a realistic mean state could produce the correct sign of surface flux anomalies relative to intraseasonal precipitation, which helps destabilize local intraseasonal disturbances (e.g., Maloney and Esbensen 2005, hereafter ME05). As seen in Fig. 8, the amplitude of anomalous southwesterly winds at 850 hPa associated with enhanced convection of the leading ISV mode over the ENP is about 2 m s^{-1}. Therefore, under a westerly or weak easterly environmental summer mean flow, this anomalous southwesterly ISV wind will facilitate a positive feedback for the growth of ISV disturbances. Namely, stronger ISV convection over the ENP will lead to increased low-level southwesterly winds; this increased southwesterly low-level wind will further lead to enhanced surface latent heat fluxes (LHF) under westerly or weak easterly flow, thus supporting tropospheric moisture anomalies and giving rise to intensification of ISV convection. On the contrary, with the presence of a strong mean easterly low-level wind, southwesterly anomalous wind in response to enhanced ISV convection will reduce LHFs and dampen the existing ISV convective disturbances by weakening the total easterly winds. A recent study by Rydbeck et al. (2013) also illustrated that easterly mean wind biases in a regional climate model were responsible for the inability of that model to sustain a local model intraseasonal variability over the eastern Pacific warm pool, creating the incorrect sign of the latent heat flux anomalies relative to anomalous precipitation and column water vapor anomalies.

To substantiate the above hypothesis, we further analyze LHF anomalies associated with the ISV over the ENP. Similar to Fig. 7, Fig. 10 illustrates simultaneous regression patterns (i.e., day 0) of 30–90-day bandpass-filtered LHF (shaded) and 850-hPa wind anomalies (vectors) against rainfall anomalies over the ENP box region from both observations and GCM simulations. (Note that since results for the two versions of HadGEM2, IPSL-CM5A, and MIROC-ESM models greatly resemble each other, only results based on one version of these GCMs are presented in Fig. 10. Also, daily surface latent heat flux data were not available for CCSM4.0 and HadCM3, and so results from these models are not shown in Fig. 10.) In agreement with previous findings by ME05, enhanced LHF anomalies are found over convectively active regions of the ISV (cf. Figs. 8a, 10a at day 0). Meanwhile, maximum positive LHF anomalies tend to be collocated with the maximum anomalous wind speed (Fig. 10a), further suggesting the potentially critical role of anomalous wind to the surface LHF anomalies, as proposed by ME05. Thus, this

configuration of anomalous surface wind, LHF, and convection represents a positive feedback process to sustain the ENP ISV convection as previously described. These features are reasonably well simulated in CNRM-CM5, CSIRO-Mk3, HadGEM2-CC, MPI-ESM-LR, and MRI-CGCM3, consistent with relatively better skill in simulating ISV in these GCMs. Much stronger amplitudes in LHF anomalies relative to observations are noted in CNRM-CM5 and HadGEM2-CC, in agreement with the stronger ISV convection and associated wind anomalies in these two models. On the other hand, anomalous LHF patterns over the ENP simulated in several other GCMs are not as well organized as in the observations, including GFDL-ESM2M, INM-CM4, IPSL-CM5A-LR, MIROC-ESM, and NorESM1-M. As previously mentioned, these models are characterized by strong easterly summer mean flow at 850 hPa over the ENP and also exhibit poor skill in representing the ENP ISV in general. As an example using INM-CM4 (Fig. 10g), although this model reasonably captures the low-level anomalous wind pattern corresponding to enhanced convection over the ENP (cf. vectors in Figs. 10a,g), because of the presence of the easterly mean flow in the model, negative (positive) LHF anomalies are found to be associated with westerly (easterly) wind anomalies. As a result, the strong negative LHF anomalies over ISV convectively active regions will weaken the initial ISV convection. While surface wind speed data are needed for an accurate diagnosis of the surface LHF budget, the results presented in this part strongly suggest that a realistic mean flow in the model will greatly benefit its simulation of the ENP ISV through a realistic representation of the anomalous LHF pattern and its feedback to ISV convection.

We cannot discount other reasons for why some models produce more realistic eastern Pacific intraseasonal variability than others, including improved convection parameterizations (e.g., Kim et al. 2009; Jiang et al. 2012), nor can we discount that the improved mean state is a result of improved intraseasonal variability that rectifies onto the low-level mean winds. However, our results at least strongly suggest an important role for a realistic depiction of low-level mean winds and their modulation of surface latent heat flux anomalies in producing more realistic intraseasonal variability in climate models, a result also supported by comparing the results of Small et al. (2011) and Rydbeck et al. (2013), in which the same regional coupled model run with different mean states is shown to produce substantially different eastern Pacific intraseasonal variability. We note no obvious relationship between horizontal resolution (Table 1) and the ability to produce realistic intraseasonal variability. For example, CCSM4.0 is among one of the
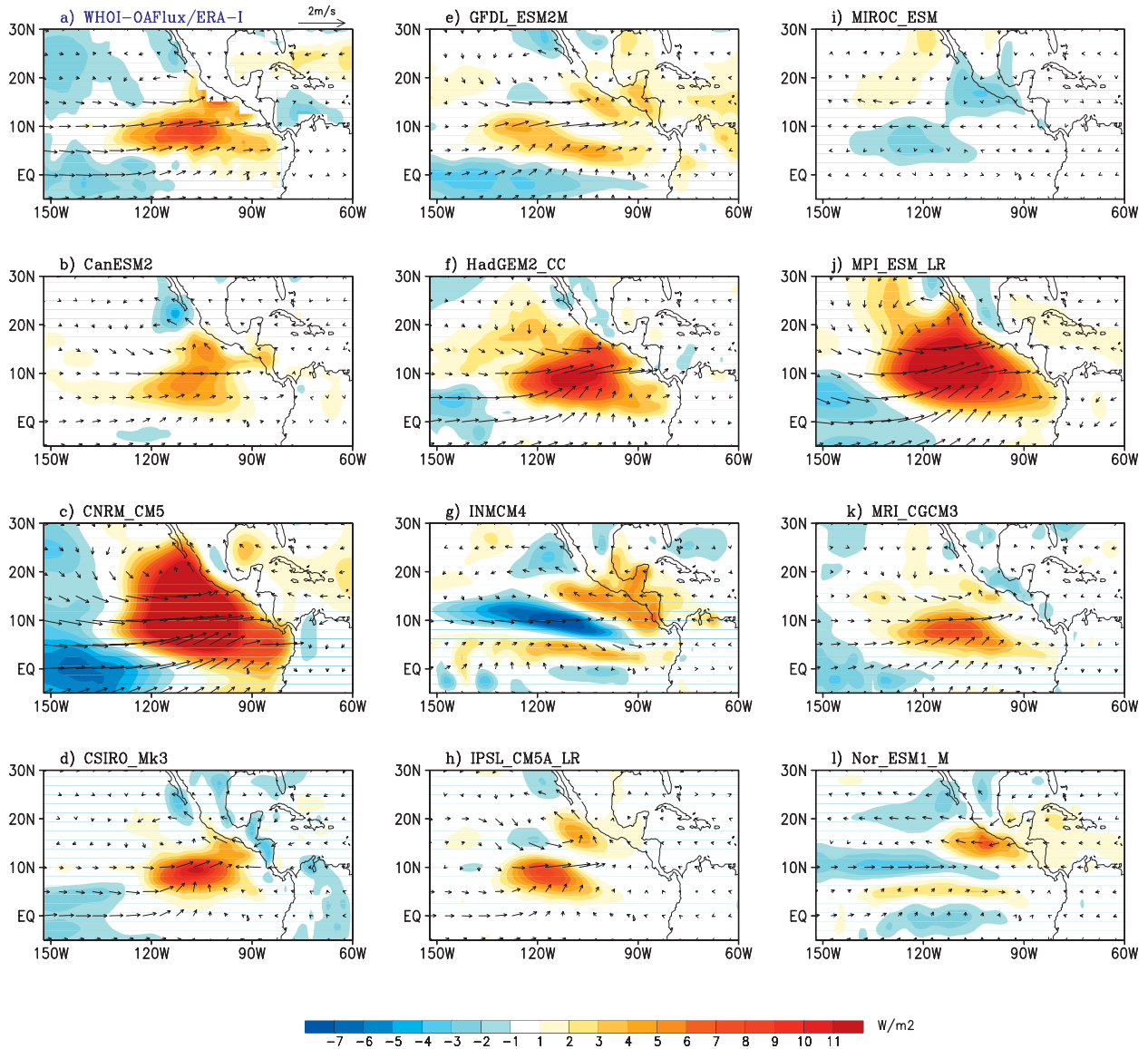
FIG. 10. Simultaneous regression patterns (i.e., day 0) of anomalous surface latent heat flux (shaded) and 850-hPa winds (vectors) against the corresponding rainfall anomalies over the ENP box (7.5°–15°N, 110°–100°W) in (a) observations and (b)–(l) model simulations.

higher-resolution models but simulates variability very unrealistically, whereas HadCM3 is one of the coarsest but produces one of the best variability simulations. This is largely in agreement with a previous study by Jiang et al. (2012), in which they demonstrated that GCM fidelity in simulating the 40-day ENP ISV mode seems not sensitive to model horizontal resolution, whereas increased resolution could be helpful for representing the QBM mode over the ENP.

4. Future projection of the ISV over the ENP

In this section, future changes in characteristics of the ENP ISV are further explored by analyzing output

based on three GCMs, HadGEM2-CC, HadGEM2-ES, and MPI-ESM-LR for the period of 2076–99 under the RCP8.5 projection pathway. These are the only models that have daily rainfall output available under the RCP8.5 projection scenario in the CMIP5 data portal at the time of this analysis and meanwhile exhibit relatively good simulation for ENP ISV.

Figure 11 illustrates projected changes in summer mean rainfall patterns over the ENP for the period of 2076–2100 under the RCP8.5 scenario relative to the present day climate (1981–2005) based on the three GCM simulations. Simulations based on these three GCMs exhibit good agreement with each other in that
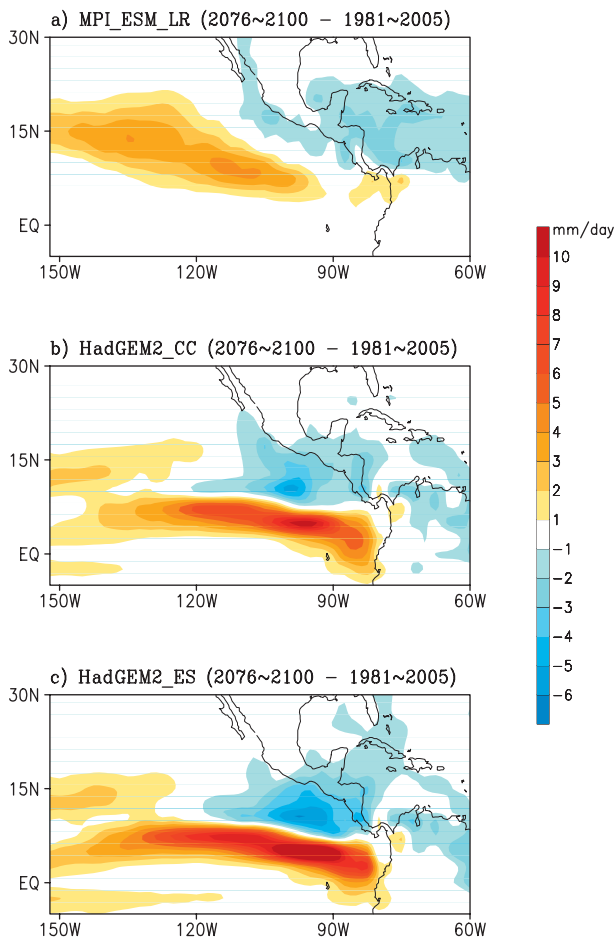
FIG. 11. (a)–(c) Projected changes in summer mean rainfall patterns between the period of 2076–99 under the RCP8.5 projection scenario and 1981–2005 based on historical simulations.
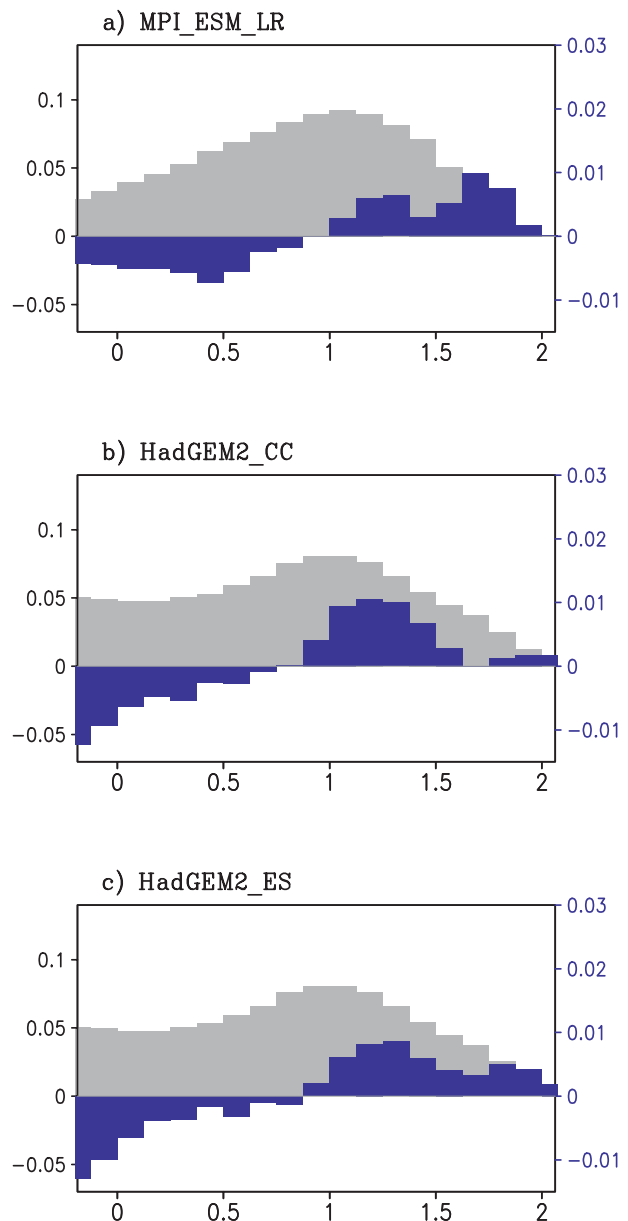

FIG. 12. (a)–(c) The PDF of summer rainfall as a function of rain rate over the ENP (5°–15°N, 130°–90°W) based on historical simulations (1981–2005) from three GCMs: HadGEM2-CC, HadGEM2-ES, and MPI-ESM-LR (reproduced from Fig. 3) (gray shading with left axes). Changes in rainfall PDFs in future projections (2076–99) under the RCP8.5 projection scenario (blue shading with right axes). The precipitation rate on *x* axis is plotted on a log scale.

summertime precipitation is projected to be reduced in the northern part of the ENP warm pool and the Caribbean. Precipitation is projected to be enhanced over the southern part of the ENP between 5°N and 10°N, particularly in simulations based on HadGEM2-CC and HadGEM2-ES, suggesting a strengthening and southward shift of the ENP ITCZ. The positive rainfall change in MPI-ESM-LR is displaced slightly northward and smaller in amplitude relative to that in both Hadley Centre models. This projected change in summertime rainfall over the ENP and adjacent regions is generally in agreement with results based on a 15-member model ensemble described in Part III of the overview paper that summarizes the NOAA CMIP5 Task Force's efforts in assessing the North American climate in CMIP5 models (E. D. Maloney et al. 2012, unpublished manuscript). These results are also consistent with changes in mean summertime precipitation in the eastern Pacific and Caribbean documented for CMIP3 models (e.g., Neelin et al. 2006).

Figure 12 further demonstrates projected changes in rain-rate PDFs under the RCP8.5 scenario in the three GCMs. The background gray bars in each panel denote rainfall PDFs over the ENP during the period of 1981–2005, which are duplicated from Fig. 3, while blue bars represent rainfall PDF changes in the future climate relative to that under the current climate (see
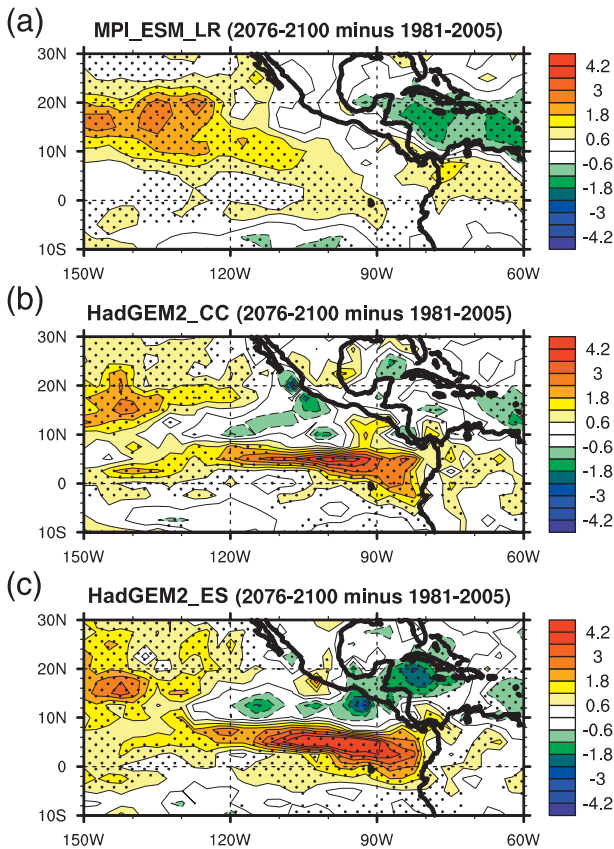
FIG. 13. Difference in the STD of the 10–90-day bandpass-filtered precipitation between the two periods of 2076–2100 and 1981–2005 in the (a) MPI-ESM-LR, (b) HadGEM2-CC, and (c) HadGEM2-ES models (mm day^{-1}). Stippling shows where the variance difference is significantly different from zero at the 95% confidence level using a chi-squared test.

axes on the right). Relative to today's climate, all three GCMs project an increase in the frequency of heavy rain (>10 mm day^{-1}) and a decrease in occurrence of light rain.

Next, we examine how ISV over the ENP changes in the RCP8.5 scenario based on the three aforementioned GCM simulations. Figure 13 illustrates differences in STD patterns of 10–90-day bandpass-filtered rainfall between the two periods of 2076–2100 and 1981–2005. Largely mimicking the mean precipitation changes shown in Fig. 11, a significant increase in rainfall STD between 5° and 10°N is noted in the ENP for all models. Significance is determined at the 95% confidence level using a chi-squared test. Interestingly, these models also exhibit significant decreases in intraseasonal variability in the northern part of the ENP off the coast of Mexico/Central America and the Caribbean.

In Fig. 14, we illustrate the spatial amplitude of the leading CEOF mode of summertime rainfall over the ENP simulated in the three GCMs for the period of 2076–2100. To facilitate the comparison, the spatial

amplitude of CEOF1 derived from historical simulations in these three models is also shown in Fig. 14; the changes in the CEOF1 amplitude between the two periods are displayed in the lower panels. Largely consistent with the projected changes in patterns of summer mean rainfall and the STD of 10–90-day filtered rainfall, amplitude increases of the leading CEOF are exhibited on the southern fringe of the original CEOF amplitude maximum in all three GCMs for the RCP8.5 scenario. Changes in the spatial phase of the leading CEOF mode among models are rather small and thus are not shown here.

5. Summary and discussion

As one of the dominant forms of the tropical atmospheric variability, intraseasonal variability over the eastern North Pacific Ocean exerts pronounced influences on regional weather and climate and hence provides a primary source for extended-range climate prediction. Moreover, as GCMs have become essential tools for prediction and projections of future climate, current model deficiencies in representing this fundamental component of atmospheric variability leave us greatly disadvantaged in climate change studies. As a part of collective efforts coordinated by the NOAA MAPP program's CMIP5 Task Force to assess North American climate simulated in CMIP5 models, we have evaluated model fidelity in representing ENP ISV in 16 GCMs participating in the CMIP5 project. Among the 16 CMIP5 GCMs examined in this study, only seven GCMs capture the spatial pattern of the leading ISV mode over the ENP reasonably well, although even these GCMs exhibit biases in simulating ISV amplitude.

Analyses further indicate that model fidelity in representing the ENP ISV in a GCM is closely associated with its ability to simulate a realistic summer mean state. The presence of a westerly or very weak easterly low-level mean wind over the ENP warm pool region in a model, as in the observations, appears conducive to more realistic simulation of eastern Pacific ISV. One hypothesis is that a realistic mean state could produce the correct sign of surface flux anomalies relative to the ISV convection, which helps to destabilize local intraseasonal disturbances through a positive feedback between convection and wind-induced surface latent heat fluxes, as proposed by ME05. When strong easterly mean low-level flow is present over the ENP in the biased models, southwesterly wind anomalies in response to the enhanced convection will lead to local negative latent heat flux anomalies, thus weakening the existing ISV disturbances. This hypothesis does not rule out other reasons for better variability in some models, such as improved parameterizations of deep convection.
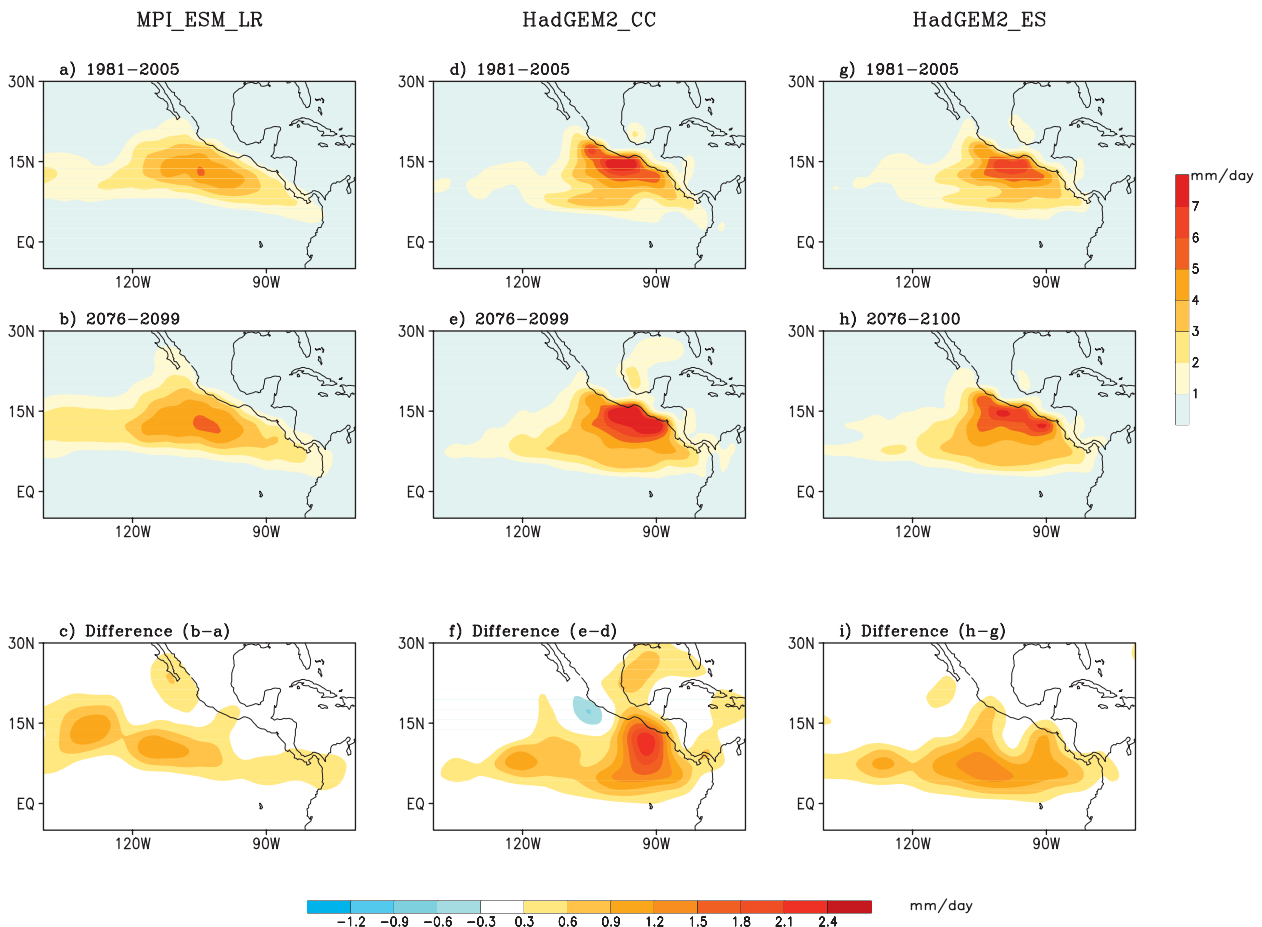
FIG. 14. Spatial distributions of the CEOF1 amplitude of summer rainfall over the ENP based on three CMIP5 models in [(a),(d), and (g)] historical simulations, [(b),(e), and (h)] future projections under the RCP8.5 scenario, and [(c),(f), and (i)] their differences.

Projected changes in the characteristics of ENP ISV under the RCP8.5 projection pathway are also explored in simulations from three CMIP5 GCMs. Consistent with the future change in the summer mean rainfall pattern, analyses based on these three CMIP5 models project that the amplitude of ISV will be enhanced over the southern part of the ENP between 5° and 10°N, while reduced over the northern ENP off the coastal region of Mexico/Central America and the Caribbean.

It is noteworthy that, despite the traditional notion of ENP ISV as being a local expression of the global MJO, the observed linkage between the intraseasonal variability over the ENP and western Pacific is only captured in two GCMs. While ENP ISV is reasonably well represented in several other GCMs, it tends to be independent from triggering from the west based on these simulations. These results are in general agreement with several recent studies and indicate that ENP ISV may represent a regional mode of variability over the eastern Pacific warm pool that can exist in isolation from the

Eastern Hemisphere given the local eastern Pacific environmental setting during boreal summer (see also Jiang et al. 2012; Rydbeck et al. 2013). For a future study, it would be interesting to explore the percentage of ENP ISV events that are associated with eastward-propagating MJO signals from the Eastern Hemisphere in the observations.

Our preliminary analyses illustrate that the several GCMs that exhibit relatively higher skill at simulating ENP ISV also show good performance in simulating MJO activity over the Indian and western Pacific Ocean, including CNRM-CM5, MPI-ESM-LR, and MRI-CGCM3 (figure not shown). Although the three Hadley Centre GCMs (HadCM3, HadGEM2-CC, and HadGEM2-ES) are among the top models in simulating ENP ISV (see Fig. 7), they produce relatively weak MJO signals. Moreover, although the two MIROC-ESM models fail to simulate realistic ENP ISV (see Figs. 7, 9), they capture the eastward propagation associated with the MJO over the Indian Ocean/western Pacific (not shown) well. While

detailed examination of the global MJO simulations in the CMIP5 GCMs has been reported in other studies (e.g., Hung et al. 2013) and is beyond the scope of this study, the inconsistencies in simulations of the MJO and ENP ISV in several GCMs could be partially caused by the great sensitivity of ENP ISV to the local summer mean state in a GCM in addition to model physics.

This study mainly focused on the leading ISV mode (40-day mode) over the ENP. The second ISV mode over the ENP (a quasi-biweekly mode) was not included in this analysis because of its small spatial scale and, thus, more difficulty the relatively coarse-resolution CMIP5 models have at resolving this feature. Moreover, convection over the eastern Pacific warm pool region during boreal summer is characterized by active synoptic-scale systems, including easterly waves and Rossby and Kelvin waves, as well as hurricanes. Therefore, a comprehensive examination of processes associated with the ENP ISV has to be performed within a multiscale framework. Future investigation is warranted to understand the importance of upscale effects from synoptic-scale convection systems for sustaining ENP ISV and how these processes are represented in current GCMs.

REFERENCES

Barnett, T. P., 1983: Interaction of the monsoon and Pacific trade-wind system at interannual time scales. 1. The equatorial zone. *Mon. Wea. Rev.,* **111,** 756–773.

Chou, S.-H., E. J. Nelkin, J. Ardizzone, R. Atlas, and C.-L. Shie, 2001: Goddard Satellite-based Surface Turbulent Fluxes (GSSTF): Version 2 documentation. Goddard Earth Sciences Data and Information Services Center, Greenbelt, Maryland. [Available online at http://disc.sci.gsfc.nasa.gov/precipitation/data-holdings/access/gsstf2.0.shtml.]

Dee, D. P., and Coauthors, 2011: The ERA-Interim reanalysis: Configuration and performance of the data assimilation system. *Quart. J. Roy. Meteor. Soc.,* **137,** 553–597, doi:10.1002/qj.828.

Higgins, R. W., and W. Shi, 2001: Intercomparison of the principal modes of interannual and intraseasonal variability of the North American Monsoon System. *J. Climate,* **14,** 403–417.

Horel, J. D., 1984: Complex principal component analysis: Theory and examples. *J. Climate Appl. Meteor.,* **23,** 1660–1673.

Huffman, G. J., R. F. Adler, B. Rudolf, U. Schneider, and P. R. Keehn, 1995: Global precipitation estimates based on a technique for combining satellite-based estimates, rain-gauge analysis, and NWP model precipitation information. *J. Climate,* **8,** 1284–1295.

Hung, M., J. Lin, W. Wang, D. Kim, T. Shinoda, and S. Weaver, 2013: MJO and convectively coupled equatorial waves simulated by CMIP5 climate models. *J. Climate,* in press.

Inness, P. M., and J. M. Slingo, 2003: Simulation of the Madden–Julian oscillation in a coupled general circulation model. Part I: Comparison with observations and an atmosphere-only GCM. *J. Climate,* **16,** 345–364.

Jiang, X., and D. E. Waliser, 2008: Northward propagation of the subseasonal variability over the eastern Pacific warm pool. *Geophys. Res. Lett.,* **35,** L09814, doi:10.1029/2008GL033723.

——, and ——, 2009: Two dominant subseasonal variability modes of the eastern Pacific ITCZ. *Geophys. Res. Lett.,* **36,** L04704, doi:10.1029/2008gl036820.

——, T. Li, and B. Wang, 2004: Structures and mechanisms of the northward propagating boreal summer intraseasonal oscillation. *J. Climate,* **17,** 1022–1039.

——, and Coauthors, 2012: Simulation of the intraseasonal variability over the eastern Pacific ITCZ in climate models. *Climate Dyn.,* **39,** 617–636, doi:10.1007/s00382-011-1098-x.

Kim, D., and Coauthors, 2009: Application of MJO simulation diagnostics to climate models. *J. Climate,* **22,** 6413–6436.

——, A. H. Sobel, E. D. Maloney, D. M. W. Frierson, and I. S. Kang, 2011: A systematic relationship between intraseasonal variability and mean state bias in AGCM simulations. *J. Climate,* **24,** 5506–5520.

——, ——, A. D. Del Genio, Y. Chen, S. J. Camargo, M.-S. Yao, M. Kelley, and L. Nazarenko, 2012: The tropical subseasonal variability simulated in the NASA GISS general circulation model. *J. Climate,* **25,** 4641–4659.

Lin, J.-L., and Coauthors, 2006: Tropical intraseasonal variability in 14 IPCC AR4 climate models. Part I: Convective signals. *J. Climate,* **19,** 2665–2690.

——, B. E. Mapes, K. M. Weickmann, G. N. Kiladis, S. D. Schubert, M. J. Suarez, J. T. Bacmeister, and M. I. Lee, 2008: North American monsoon and convectively coupled equatorial waves simulated by IPCC AR4 coupled GCMs. *J. Climate,* **21,** 2919–2937.

Lorenz, D. J., and D. L. Hartmann, 2006: The effect of the MJO on the North American monsoon. *J. Climate,* **19,** 333–343.

Madden, R. A., and P. R. Julian, 1994: Observations of the 40–50-day tropical oscillation—A review. *Mon. Wea. Rev.,* **122,** 814–837.

Magana, V., J. A. Amador, and S. Medina, 1999: The midsummer drought over Mexico and Central America. *J. Climate,* **12,** 1577–1588.

Maloney, E. D., and D. L. Hartmann, 2000a: Modulation of eastern North Pacific hurricanes by the Madden–Julian oscillation. *J. Climate,* **13,** 1451–1460.

——, and ——, 2000b: Modulation of hurricane activity in the Gulf of Mexico by the Madden–Julian oscillation. *Science,* **287,** 2002–2004.

——, and S. K. Esbensen, 2003: The amplification of east Pacific Madden–Julian oscillation convection and wind anomalies during June–November. *J. Climate,* **16,** 3482–3497.

——, and ——, 2005: A modeling study of summertime east Pacific wind-induced ocean–atmosphere exchange in the intraseasonal oscillation. *J. Climate,* **18,** 568–584.

——, and ——, 2007: Satellite and buoy observations of boreal summer intraseasonal variability in the tropical northeast Pacific. *Mon. Wea. Rev.,* **135,** 3–19.

——, D. B. Chelton, and S. K. Esbensen, 2008: Subseasonal SST variability in the tropical eastern North Pacific during boreal summer. *J. Climate,* **21,** 4149–4167.

Martin, E. R., and C. Schumacher, 2011: Modulation of Caribbean precipitation by the Madden–Julian oscillation. *J. Climate,* **24,** 813–824.

Neelin, J. D., M. Munnich, H. Su, J. E. Meyerson, and C. E. Holloway, 2006: Tropical drying trends in global warming models and observations. *Proc. Natl. Acad. Sci. USA,* **103,** 6110–6115, doi:10.1073/pnas.0601798103.

Reynolds, R. W., T. M. Smith, C. Liu, D. B. Chelton, K. S. Casey, and M. G. Schlax, 2007: Daily high-resolution-blended analyses for sea surface temperature. *J. Climate,* **20,** 5473–5496.

Riahi, K., and Coauthors, 2011: RCP 8.5—A scenario of comparatively high greenhouse gas emissions. *Climatic Change,* **109,** 33–57, doi:10.1007/s10584-011-0149-y.

Rydbeck, A. V., E. D. Maloney, S.-P. Xie, J. Hafner, and J. Shaman, 2013: Remote forcing versus local feedback of east Pacific intraseasonal variability. *J. Climate,* in press.

Serra, Y. L., G. N. Kiladis, and K. I. Hodges, 2010: Tracking and mean structure of easterly waves over the Intra-Americas Sea. *J. Climate,* **23,** 4823–4840, doi:10.1175/2010JCLI3223.1.

Slingo, J. M., and Coauthors, 1996: Intraseasonal oscillations in 15 atmospheric general circulation models: Results from an AMIP diagnostic subproject. *Climate Dyn.,* **12,** 325–357.

Small, R. J., S. P. De Szoeke, and S.-P. Xie, 2007: The Central American midsummer drought: Regional aspects and large-scale forcing. *J. Climate,* **20,** 4853–4873.

——, S. P. Xie, E. D. Maloney, S. P. de Szoeke, and T. Miyama, 2011: Intraseasonal variability in the far-east Pacific: Investigation of the role of air–sea coupling in a regional coupled model. *Climate Dyn.,* **36,** 867–890, doi:10.1007/s00382-010-0786-2.

Sperber, K. R., S. Gualdi, S. Legutke, and V. Gayler, 2005: The Madden–Julian oscillation in ECHAM4 coupled and uncoupled general circulation models. *Climate Dyn.,* **25,** 117–140, doi:10.1007/s00382-005-0026-3.

Taylor, K. E., 2001: Summarizing multiple aspects of model performance in a single diagram. *J. Geophys. Res.,* **106,** 7183–7192.

——, R. J. Stouffer, and G. A. Meehl, 2012: An overview of CMIP5 and the experiment design. *Bull. Amer. Meteor. Soc.,* **93,** 485–498.

Thayer-Calder, K., and D. A. Randall, 2009: The role of convective moistening in the Madden–Julian oscillation. *J. Atmos. Sci.,* **66,** 3297–3312.

Waliser, D. E., 2012: Predictability and forecasting. *Intraseasonal Variability in the Atmosphere–Ocean Climate System,* 2nd ed. W. K. M. Lau and D. E. Waliser, Eds., Springer, 433–476.

——, and Coauthors, 2003: AGCM simulations of intraseasonal variability associated with the Asian summer monsoon. *Climate Dyn.,* **21,** 423–446, doi:10.1007/s00382-003-0337-1.

Wu, M. L. C., S. D. Schubert, M. J. Suarez, and N. E. Huang, 2009: An analysis of moisture fluxes into the Gulf of California. *J. Climate,* **22,** 2216–2239.

Yu, L., X. Jin, and R. A. Weller, 2008: Multidecade Global Flux Datasets from the Objectively Analyzed Air-sea Fluxes (OAFlux) Project: Latent and sensible heat fluxes, ocean evaporation, and related surface meteorological variables. Tech. Rep. OA-2008-01, 64 pp. [Available online at http://oaflux.whoi.edu/pdfs/OAFlux_TechReport_3rd_release.pdf.]

Zhu, H. Y., H. Hendon, and C. Jakob, 2009: Convection in a parameterized and superparameterized model and its role in the representation of the MJO. *J. Atmos. Sci.,* **66,** 2796–2811.